Viscoelastic Ligament Dynamics in Free Liquid Jet Experiments

Christophe Tirel, Marie-Charlotte Renoult, Christophe Dumouchel

▶ **To cite this version:**

Christophe Tirel, Marie-Charlotte Renoult, Christophe Dumouchel. Viscoelastic Ligament Dynamics in Free Liquid Jet Experiments. International Conference on Liquid Atomization and Spray Systems, Jul 2018, Chicago, United States. hal-01844090

HAL Id: hal-01844090

https://normandie-univ.hal.science/hal-01844090

Submitted on 19 Jul 2018

HAL is a multi-disciplinary open access archive for the deposit and dissemination of scientific research documents, whether they are published or not. The documents may come from teaching and research institutions in France or abroad, or from public or private research centers.

L'archive ouverte pluridisciplinaire **HAL**, est destinée au dépôt et à la diffusion de documents scientifiques de niveau recherche, publiés ou non, émanant des établissements d'enseignement et de recherche français ou étrangers, des laboratoires publics ou privés.

Viscoelastic ligament dynamics in free liquid jet experiments

C. Tirel[1], M. C. Renoult[1], C. Dumouchel[1]
[1]CORIA, Normandie Université, Université et INSA de Rouen, CNRS, France

Abstract

The widely-used experimental methods to determine the relaxation time of viscoelastic solutions are based on ligament thinning measurements. The CaBER (Capillary Breakup Extensional Rheometer) produces a stretched liquid filament between two plates and deduces the solution relaxation time from its diameter temporal decrease. However this technique does not suit dilute polymer solutions for which the jet rheometer such as the ROJER (Rayleigh Ohnesorge Jetting Extensional Rheometer) is seen as a promising alternative. The measurement principle consists in analyzing the temporal evolution of the neck diameter of a liquid jet experiencing a capillary instability. However, this technique is known to be difficult to implement and has revealed a dependence between the measured relaxation time and the operating conditions involving the jet velocity, the perturbation frequency and initial amplitude.
In the present work an experimental protocol is reported to extract the relaxation time of a dilute polymer solution from its jet behavior. The main features are the use of free liquid jets which simplifies the control of the operating conditions and of a multi-scale analyzing tool which simplifies the measurement to be performed on the jets. Twenty one experiments with various jet diameters and velocities were performed. The results explain why the relaxation time measurement cannot be performed on any jets and allow elaborating a precise procedure for a confident measurement of the relaxation time.

Keywords: dilute polymer solution, ligament behavior, jet break-up

---

Introduction

Viscoelastic liquids have specific shear thinning and strain-hardening properties that confer on them characteristic behaviors while atomizing. For instance, laminar viscoelastic liquid jets break up with formation of beads-on-strings structures composed of large spherical beads and thin cylindrical threads. These threads might be the seat of an elongational flow where capillary and elastic forces are in balance, the first being the driving force, the second the resistive one, that leads to a specific decrease of their diameter with time. This decrease is controlled by the stress relaxation time scale t_r of the viscoelastic solution. The knowledge of this time scale is therefore of paramount importance in the context of atomization but its experimental determination remains challenging especially for very dilute polymer solutions.
The Capillary Breakup Extensional Rheometer (CaBER) performs this measurement by detecting and analyzing the elasto-capillary thinning of a filament formed by stretching a liquid bridge between two coaxial cylindrical plates. For dilute polymer solutions, Rodd and al. [1] have shown that the CaBER have limitations: there is a lower shear viscosity limit and a lower relaxation time limit for which the relaxation time measurement is not possible due to the fast thinning of the filament and the lack of resolution of the device. Moreover, liquid shape oscillations are introduced due to the fast transition of the plates from their initial positions to their final configurations for which the liquid bridge is unstable and thins down [2]. These oscillations persist for multiples of the capillary time and corrupt the CaBER measurement if the breakup occurs before they vanish. These limitations have been overcome in part with the use of the Slow Retraction Method and the use of a high speed camera, but there is a progressive appearance of beads-on-strings structures at the final steps of the filament thinning resulting from an iterated elastic instability [3].
Another technic based on jet experiments have been developed [4-8]. For dilute polymer solutions, the jet rheometer is seen as a promising alternative to the liquid filament rheometer [7]. Up so far, the jet rheometer considers the behavior of a cylindrical liquid jet forced at a given perturbation amplitude and frequency [4-6, 8]. However, this technic remains tricky in particular because the resulting relaxation time might report a dependence on the jet operating conditions, i.e. the jet velocity and the initial disturbance amplitude and frequency [6]. Recently, new results suggest however the existence of an operating domain free of these dependences [8].

The present work intends to shed more light on the use of liquid jet capillary instability as a support to perform relaxation time measurement. Two characteristic features distinguish the present approach: 1 – the use of free liquid jets; 2 – the application of a multi-scale tool for analyzing the jets.

During the capillary instability of a viscoelastic cylindrical jet, the neck diameter $D_{min}(t)$ is expected to decrease according to three regimes that are presented in Table 1. The first regime is the Plateau-Rayleigh (PR) instability during which a sinusoidal perturbation develops and $D_{min}(t)$ decreases according to Eq. (1) where D_{jet} is the jet diameter, ω the non-dimensional growth rate and t_σ the capillary time (= $(\rho D_{jet}^3/\sigma)^{1/2}$ ρ being the liquid density and σ the surface tension) [9]. The second regime is the Elasto-Capillary (EC) regime during which elastic and capillary forces balance in the liquid strings whose diameter $D_{min}(t)$ exhibits an exponential decrease as reported by Eq. (2). The third regime is the Visco-Capillary (VC) regime during which elongational viscous and capillary forces balance in the liquid string. This mechanism is associated with a linear decrease of the neck diameter $D_{min}(t)$ (see Eq. (3) where t_{BU} designates the jet breakup time and μ_e the terminal elongational viscosity. This presentation shows that the measurement of the relaxation time t_r is possible provided that 1 – the EC regime exists; 2 – the temporal resolution is high enough to provide a exploitable $D_{min}(t)$ in this regime.

Regime 1: Plateau-Rayleigh (PR)	**Regime 2:** Elasto-Capillary (EC)	**Regime 3:** Visco-Capillary (VC)
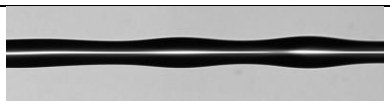	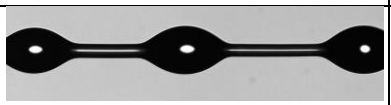	
$D_{jet} - D_{min}(t) \propto exp\left(\omega \frac{t}{t_\sigma}\right)$ (1)	$D_{min}(t) \propto exp\left(-\frac{t}{3t_r}\right)$ (2)	$D_{min}(t) \propto \frac{\sigma}{\mu_e}(t_{BU} - t)$ (3)

Table 1 Successive regimes of a viscoelastic jet capillary instability

Based on the behaviors summarized in Table 1, previous jet rheometers rested on the measurement of $D_{min}(t)$ which required the determination of its location. The present work uses a different approach through the application of a multi-scale analysis as introduced in previous papers [10,11]. This analysis describes the jet as a time-dependent scale distribution $e_2(d,t)$ and the analysis consists in considering the behavior of a small scale whose dynamics is the same as the diameter $D_{min}(t)$. The analysis of this dynamics allows identifying the existence of the EC regime and, then, measuring the solution relaxation time.

Compared to the previous works [10,11], the optical arrangement in the present work has been modified in order to improve the spatial resolution. It is indeed of paramount importance to have, at each time, enough scales (that is enough pixels) to correctly describe the ligaments that are the structures of interest in this study. Furthermore, by assuming the axisymmetry of the jets, the multi-scale analysis is performed in 3D which returns the temporal evolution of the specific area (amount of surface area per unit volume) of the jet. Finally, new injection conditions are considered here. More precisely, three discharge orifices with different diameters have been used.

This article is structured as followed. The experimental setup and optical imaging arrangement are presented in the next section. It is followed by a section dedicated to the analyzing tools (image analysis and multi-scale analysis). Then, the results are presented and discussed. The article ends with a conclusion section.

Experimental setup

The experimental setup produces free falling cylindrical jets. The injector is composed of a cylindrical body (5 mm internal diameter) ended with a cylindrical discharge orifice of length L_{or} = 300 µm. Three different discharge orifice diameters are available, i.e., D_{or} = 200 µm, 105 µm and 42 µm. The injector is fed by a syringe pump that imposes the injection flow rate. The volume liquid flow rate Q_v is varied for each nozzle diameter in the same Reynolds number range, i.e., $Re = 4\rho Q_v/\pi D_{or}\mu \in [110; 715]$ where μ is the solution shear viscosity. (For each nozzle, seven flow rates are explored.) To visualize the total length of the jets, i.e., from the nozzle exit down to the breakup point, a 3D displacement system is used to translate the injector.

The low-viscosity viscoelastic polymer solution used contains 5 ppm of Poly(ethylene oxide) (PEO) dissolved into an aqueous mixture with 5% in mass of isopropyl alcohol (density ρ = 989 kg/m^3; shear viscosity μ = 1.34 mPa.s; surface tension σ = 48.9 mN/m). The average molar mass of the PEO is M_v = 8 10^3 kg/mol.

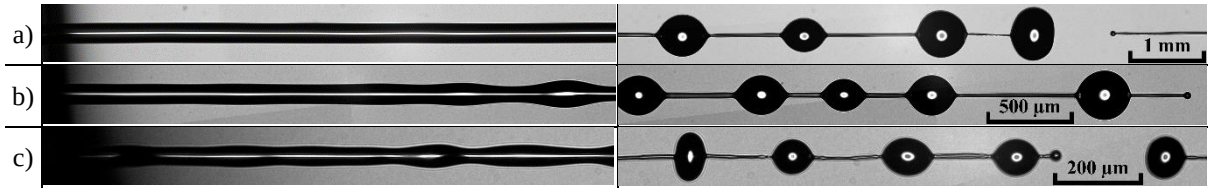

Figure 1 Viscoelastic jets at the nozzle exit and in the breakup region. a) D_{or} = 200 µm, Q_v = 5.5 ml/min; b) D_{or} = 105 µm, Q_v = 2.72 ml/min; c) D_{or} = 42 µm, Q_v = 1.54 ml/min

Transmission images of the jets are performed. In order to get a high spatial resolution, a 29 Mpixels camera (6576 x 4384 pixels, SVS-Vistek HR29050) is used. The spatial resolution has been settled to 1.26 µm/pixel for the

200 µm discharge orifice and to 0.56 µm/pixel for the 105 and 42 µm discharge orifices. The choice of these resolutions results from a compromise between the number of pixels in the jets and the depth of field of the optical arrangement. The physical field covered by the image is 8.29 mm x 5.52 mm and 3.68 mm x 2.46 mm according to the spatial resolution. For each operating condition (orifice diameter, flow rate, position) n = 150 uncorrelated images are recorded. This number is high enough for a statistical analysis as detailed in the analysis section.
Figure 1 presents typical images of the jets at the nozzle exit and in the breakup region for each orifice diameter. In the near nozzle region, the white line in the middle of the jets attests that the flows are laminar and axisymmetric. The appearance of the naturally-selected sinusoidal perturbation downstream from the nozzle is always clearly visible as well as the ligaments of the beads-on-strings pattern down to the breakup region.

Analysis

Viscoelastic flows issuing from a cylindrical orifice might be larger or smaller than the orifice diameter according to the characteristics of the internal flow. This is the reason why it is decided to characterize the jets with a proper measurement of their diameter D_{jet} and of their subsequent velocity V_{jet}. For each injection flow rate, D_{jet} is deduced from the jet projected surface area S_{jet} averaged on the 150 images and measured along a distance z_{jet} = 3 mm where the jet is not deformed, i.e., $D_{jet} = S_{jet}/z_{jet}$. The corresponding velocity is obtained by: $V_{jet} = 4Q_v/\pi D_{jet}^2$. Furthermore, the wavelength λ_{jet} of the naturally-selected mode identified in Fig. 1 is measured and averaged on 50 images for each operating condition. All these measurements are reported in Table 2.

n°	Q_v (ml/min)	D_{jet} (µm)	V_{jet} (m/s)	t_{BU} (ms)	t_σ (ms)	λ_{jet} (µm)	ω (-)
			D_{or} = 200 µm				
1.1	3.56	195	1.99	11.1	0.137	978	0.336
1.2	5.50	190	3.23	9.98	0.132	951	0.336
1.3	7.96	185	4.94	7.62	0.127	975	0.330
1.4	10.3	184	6.46	6.45	0.126	842	0.342
1.5	12.2	200	6.49	6.88	0.142	975	0.339
1.6	14.2	187	8.61	6.56	0.129	938	0.336
1.7	17.3	190	10.2	5.02	0.132	911	0.340
			D_{or} = 105 µm				
2.1	1.75	125	2.37	6.03	0.070	578	0.342
2.2	2.72	121	3.94	3.91	0.067	587	0.340
2.3	3.93	117	6.09	3.21	0.064	569	0.337
2.4	5.08	114	8.29	2.53	0.061	522	0.335
2.5	7.02	112	11.9	2.06	0.060	506	0.333
2.6	8.72	112	14.8	1.84	0.060	484	0.337
2.7	10.2	112	17.3	1.73	0.060	480	0.340
			D_{or} = 42 µm				
3.1	1.09	46.0	10.9	0.571	0.016	-	-
3.2	1.54	47.0	14.8	0.534	0.016	199	0.339
3.3	1.75	47.0	16.8	0.518	0.016	198	0.338
3.4	2.12	46.0	21.3	0.486	0.016	195	0.339
3.5	2.36	47.0	22.7	0.457	0.016	187	0.328
3.6	2.54	46.5	24.9	0.523	0.016	199	0.340
3.7	2.72	46.5	26.7	0.506	0.016	202	0.341

Table 2 Characteristics of the jets for all operating conditions
(For case n° 3.1, the wavelength measurement was not possible)

As mentioned in the introduction, a 3D multi-scale tool is used to analyze the temporal evolution of the jets. This tool has been introduced in detail in previous articles [11, 12] and is summarized here only. It provides the scale distribution $e_3(d, z)$ which is the ratio of the surface area of the local system eroded at scale d on twice the total volume of this system before any erosion operation. This distribution is measured for all possible values of the scale d (i.e., until the jet has totally disappeared by erosion) and at several locations z from the nozzle exit to the breakup region. Although images provide a 2D information, the 3D scale distribution is deduced by assuming the axisymmetry of the liquid jet at every stages. The capillary instability is known to be axisymmetric enough for this assumption to be acceptable. (This is confirmed by the images in Fig. 1.)
The steps of the scale distribution measurement are illustrated in Fig. 2. The initial image (Fig. 2-a) is treated in order to produce a two-level image (Fig. 2-b) where the liquid appears in black on a white background. Then, the

Euclidian Distance Map of the jet is performed (Fig. 2-c). The volume-based scale distribution function is calculated in a portion of the jet delimited by an Analyzing Window (Fig.2-d).

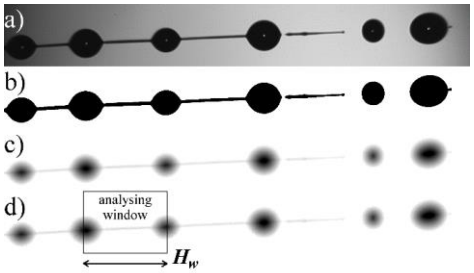

Figure 2 Steps of scale distribution measurement a) Raw image; b) Two-level image; c) Euclidian Distance Map; d) Analyzing Window where the local scale distribution is measured

The spatial evolution of the volume-based scale distribution is obtained by sliding the Analyzing Window from the nozzle exit down to the breakup region. The height *Hw* of the analyzing window is taken of the order of the naturally-selected perturbation wavelength. This choice is a good compromise between localness and number of images required to have a converged average scale distribution. Indeed, the local measurement of the scale distribution is performed on each image of the series and a local average distribution is calculated. If $e_{3i}(d,z)$ represents the measurement performed on image *i*, the average scale distribution at this location is defined by:

$$e_3(d,z) = \frac{\sum_{i=1}^{n} V_i(z)\, e_{3i}(d,z)}{\sum_{i=1}^{n} V_i(z)} \tag{4}$$

where $V_i(z)$ is the jet portion volume in the Analyzing Window in image *i*. Then, the scale distribution spatial dependence is transformed as a temporal dependence by using the equivalent time *t* defined by:

$$t = \frac{\sqrt{V_{jet}^2 + 2gz} - V_{jet}}{g} \tag{5}$$

where *g* is the gravitational acceleration. When $V_{jet}^2 >> 2gz$ (Froude number >> 1), Eq. (5) simplifies as $t = z/V_{jet}$. The temporal resolution of the scale distribution measurement is depending on the shift of the Analyzing Window. For most operating conditions, using a shift equal to H_w appeared acceptable. However, when a greater temporal resolution is required (such as for injector D_{or} = 200 µm with small injection velocities) it was divided by 2, returning twice more points.

The convergence of the mean scale distribution measurement, as a function of the image number, is studied through the value of $e_3(d=0,t)$, which is the maximum value of e_3 by definition. The variation of the average of $e_3(0,t)$ is always less than 4% when n = 150 images (this result was established for condition 1.2, 1.3, 1.5, 1.6, 2.3, 2.5, 2.6, 2.7 and for at least three different positions for every case). n = 150 is therefore a sufficient number of images.

It is important to mention that the scale distribution measured as explained above describes the mean arrangement of the liquid system. This mean arrangement is called the unit pattern of the jet. If the jet is exactly cylindrical, the unit pattern is a portion of this cylinder whatever its length ($e_3(d)$ is independent of cylinder's length). As shown in previous works ([13] for instance) $e_3(d)$ is linear in this case and decreases from $2/D_c$ at d = 0 to 0 at $d = d_{max} = D_c$ where D_c stands for the cylinder diameter. If the cylindrical jet is deformed by a sinusoidal perturbation of wavelength λ, the unit pattern is a portion of the jet of length λ. Finally, if the jet is a succession of beads connected by cylindrical ligaments, the unit pattern is made of one bead whose diameter is equal to the mean diameter of the beads seen at this location and one ligament whose diameter is equal to the mean diameter of the ligaments seen at this location. Furthermore, the bead-ligament volume ratio of the unit pattern corresponds to the mean bead-ligament volume ratio seen at this location.

An example of the temporal evolution of the scale distribution is given in Fig. 3 (Case n°1.6, refer to Table 2). At the initial time (t = 2.9 ms) $e_3(d,t)$ is linear indicating that the initial jet is cylindrical. This, of course, corresponds to the observation. As time goes, the maximum scale d_{max} (smallest scale for which $e_3(d,t) = 0$) increases in agreement with the growth of the sinusoidal perturbation in Regime 1 (see Table 1) and the behavior of the beads in Regimes 2 and 3. For the great times, note that the scale distribution remains linear in the small region. This behavior denotes the persistence of a cylindrical portion in the unit pattern which, of course, corresponds to the

string of the beads-on-strings structure. Two points are interesting to mention here: 1 – the derivative of the linear portion decreases with time which reveals the decrease of the ligament diameter (this is precisely this dynamic that we are interested in), 2 – $e_3(0,t)$ decreases with time. This second behavior is better shown in Fig. 4 for three cases (1.6; 2.6; 3.4). As mentioned earlier, $e_3(0,t)$ is half of the specific surface area (i.e. interface surface area per unit volume [14]). As expected for a capillary instability this quantity decreases with time. This behavior is reported for every case investigated in this work. (The oscillations of $e_3(0,t)$ sometimes observed at the beginning, such as for case n°1.6 in Fig. 4, are likely related to the presence of a static deformation.)

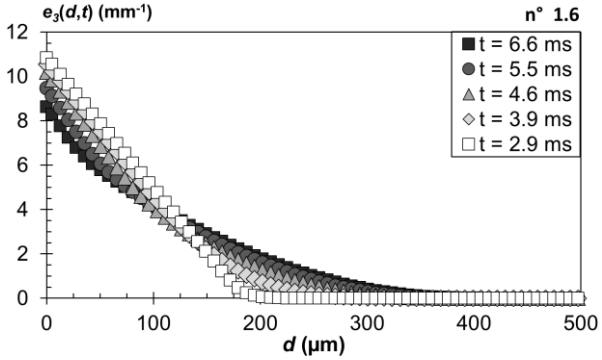

Figure 3 Temporal evolution of $e_3(d,t)$ (Case n° 1.6)

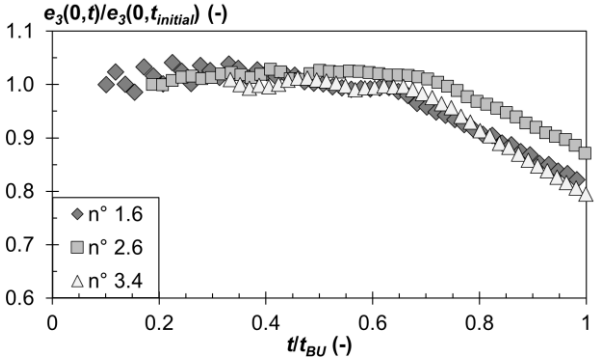

Figure 4 Temporal evolution of the specific surface $e_3(0,t)$ (Cases n° 1.6 ; 2.6 ; 3.4, the breakup times t_{BU} are given in Table 2)

Now, the analysis consists in identifying scales whose dynamics is the same as the one of the unit pattern ligaments that are the seat of an elongational flow. Using the quasi one-dimensional continuity equation provided by Stelter et al. [15], the stretching rate $\dot{\varepsilon}$ of such a flow is equal to:

$$\dot{\varepsilon} = \frac{\partial v}{\partial z} = \frac{-2}{D_c(t)} \frac{\mathrm{d}D_c(t)}{\mathrm{d}t} \tag{6}$$

where D_c is the diameter of the cylindrical ligament and v the longitudinal velocity along the z axis. It is straight forward to demonstrate that for an isolated cylinder, the stretching rate given by Eq. (6) is related to the scale distribution by [13]:

$$\dot{\varepsilon} = \frac{\dot{e_3}'(d,t)}{e_3'(d,t)} \tag{7}$$

where the prime indicates a scale derivative and the dot a temporal derivative. Since the scale distribution is linear in the scale space for a cylinder, the stretching rate characterizing its elongation is independent of the scale d also.

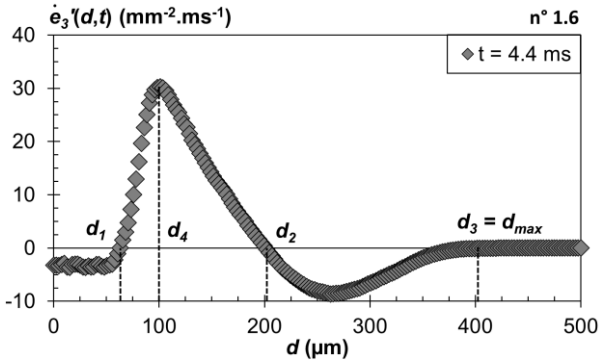

Figure 5 Temporal evolution of $\dot{e_3}'(d,t)$ (Case 1.6). Definition of characteristic scales

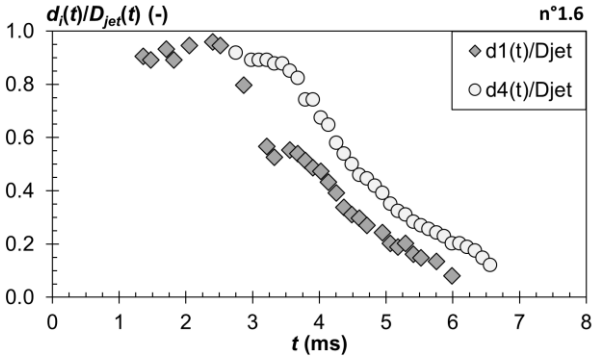

Figure 6 Temporal evolution the scales d_1 and d_4 (Case 1.6)

For case 1.6, Fig. 5 shows the function $\dot{e_3}'(d,t)$ at time t = 4.4 ms for which the jet is rearranged as beads-on-strings. This figure reveals that $\dot{e_3}'(d,t)$ is scale-independent in the small scale region, i.e., the ligament thinning is identifiable with the scale distribution temporal evolution. Furthermore, the dynamics of this flow is the same

as the dynamics of the scale d_1 defined in Fig. 5 because of the scale proximity. Therefore, as done in previous works [10-13], the temporal evolution of the necks of the jet can be explored from $d_1(t)$. However, in the present situation, an accurate determination of the scale d_1 would require a spatial resolution that is difficult to achieve when imaging the full jet. The present optical arrangement provides $d_1(t)$ measurements with non-negligible scatter (see Fig. 6 for instance) that is pejorative for the analysis. This is the reason why it is decided to consider the scale d_4 (see Fig. 5 for the definition) that is less sensitive to spatial resolution and whose dynamics remains the same as the scale d_1 as evidenced in Fig. 6.

Results and Discussion

For six cases among the 21 that constitute the experimental part of this work (see Table 2), Fig 7 presents the temporal evolution of the characteristic scale $d_4(t)$ in two different manners: $(d_4(t)/D_{jet})$ and $(1 - d_4(t)/D_{jet})$. As expected, the ratio $d_4(t)/D_{jet}$ highlights a monotonous decrease of the scale d_4. For every operating condition, the curves in Fig. 7 are used to identify the Regime 1 (PR) and the Regime 3 (VC) introduced in Table 1.

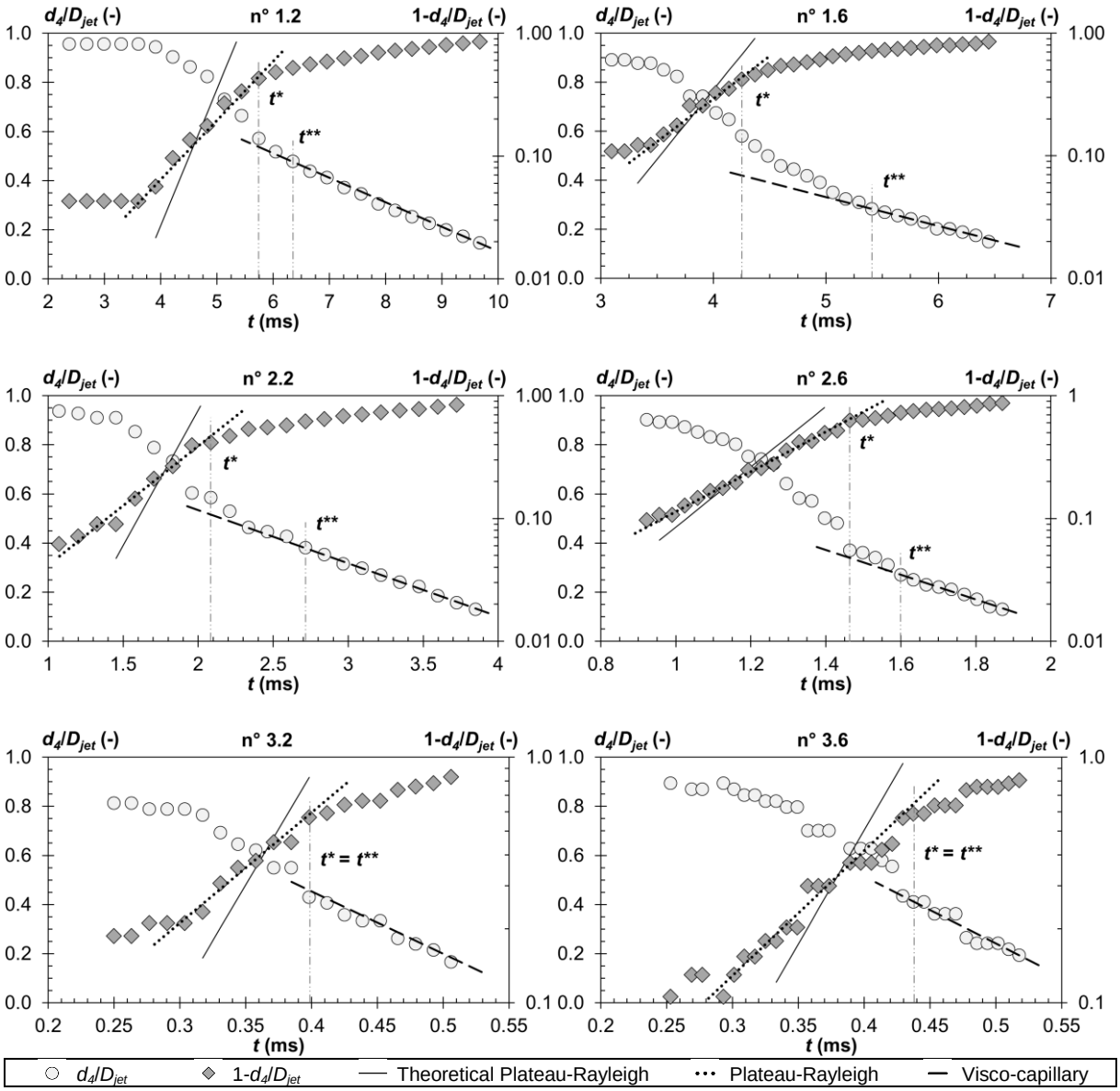

Figure 7 Temporal evolution of scale d4. Identification of Regime 1 (PR) and Regime 3 (VC) (Cases n° 1.2; 1.6; 2.2; 2.6; 3.2; 3.6)

According to Eq. (1), Regime 1 is associated with a linear increase of the function $(1 - d_4(t)/D_{jet})$ in a semi-log representation. Furthermore, being exponential (see Eq. (1)), this increase is expected to be the steepest one. This behavior is seen for every situation as evidenced by the dot lines in Fig. 7. To demonstrate that this linear increase corresponds to the PR regime, the theoretical increase expressed by Eq. (1) is calculated, ω being the non-

dimensional growth reported by Rayleigh linear theory [1] for the sinusoidal perturbation of wavelength λ. (The values of ω are given in Table 2.) The continuous lines in Fig. 7 indicate the PR theoretical results. The experimental and theoretical growth rates are of the same order of magnitude which confirms that the identified linear portion does correspond to regime 1. (The results also exhibit a systematic smaller experimental growth rate compared to the theoretical one. It is interesting to mention that this very difference was reported by the analysis of simulated capillary instability of Newtonian ligaments [12].) The time t^* at which regime 1 ends is identified as the time at which the linear behavior is lost (see Fig. 7).

According to Eq. (3), Regime 3 is associated with a linear decrease of the ratio ($d_4(t)/D_{jet}$) in a linear representation. Furthermore, this regime is the last one and should extend to the final breakup. The results presented in Fig. 7 show this behavior in every situation as indicated by the dash lines. The extension of this line allows identifying the time t^{**} from which Regime 3 starts. (The time t^{**} is shown in Fig. 7.)

The determination of the characteristic times t^* and t^{**} is performed for every operating condition and the results are displayed in Fig. 8. Following Table 1, Regime 2 – i.e. the one of interest in the present work – may extend in the interval [t^*; t^{**}] at best. Figure 8 shows that the range of this interval is very much dependent on the working conditions. For the small orifice diameter (D_{or} = 42 µm), the range of [t^*; t^{**}] is nil whatever the velocity indicating the absence of an EC regime for these jets. For the medium orifice diameter (D_{or} = 105 µm), the range of [t^*; t^{**}] remains pretty small (especially at high velocity) and might not allow the development of the EC regime. For the large orifice diameter (D_{or} = 200 µm), the range of [t^*; t^{**}] appears small for the two smallest and the highest velocities. However, for the four medium velocities (cases n° 1.3, 1.4, 1.5, 1.6), the range of [t^*; t^{**}] might be large enough to allow the development of the EC regime and, subsequently, the measurement of the relaxation time t_r.

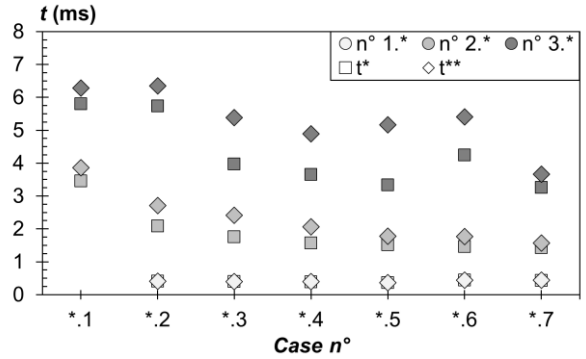

Figure 8 Characteristic times t^* and t^{**} for every working condition

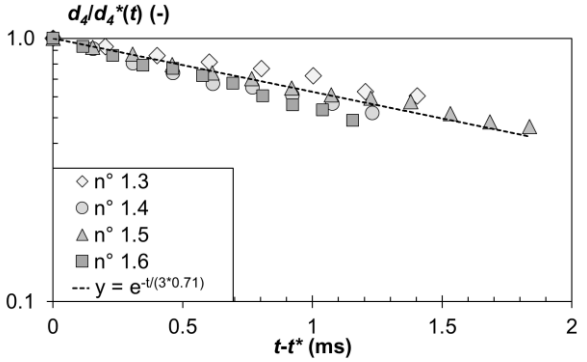

Figure 9 Evolution of $d_4(t)$ in the EC regime (Cases n° 1.3, 1.4, 1.5, 1.6)

According to Eq. (2), the measurement of the relaxation time can be performed by considering the evolution of the scale $d_4(t)$ as a function of time in a semi-log representation. In order to compare the cases with each other, the ratio $d_4(t)/d_4(t^*)$ versus $(t - t^*)$ is plotted in the interval [t^*; t^{**}] for the cases n° 1.3, 1.4, 1.5, 1.6. Figure 9 shows the results. Three important points must be mentioned. First, the four cases report a linear behavior in this representation which validates the dependence expressed by Eq. (2) and gives credit to the existence of the EC regime. Second, for every case, the number of points is sufficient to determine a slope with no ambiguity. Third, the slopes of the four cases are very close to each other. This means that the detected EC regime is not depending on the injection conditions and that the characteristic time that can be extracted from it is the relaxation time of the dilute polymer solution. For the present dilute solution, this relaxation time is t_r = 0.71 ms.

Finally, Fig. 10 shows the ratio $(t^{**} - t^*)/t_r$ for every case. It can be seen that the cases reporting an EC regime are those for which the available temporal range [t^*; t^{**}] is at least 1.5 time the relaxation time t_r. If it is less, this regime has no time to settle properly and to provide a possibility of measurement. On the other hand, we see that the jets whose breakup time are less than the relaxation time, no EC regime can be identified. This is the case of the smallest orifice diameter jets at every velocity for which the breakup time never exceeds 0.5 ms.

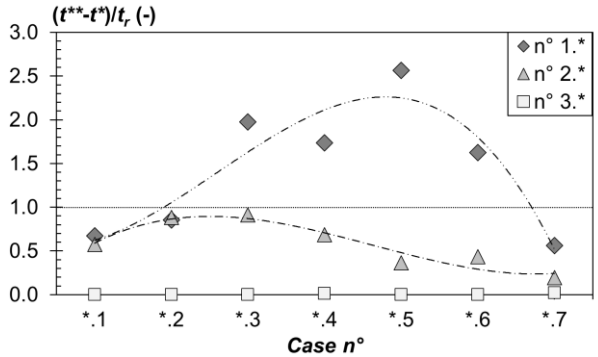

Figure 10 Comparison of the [t^*; t^{**}] range with the solution relaxation time t_r

Conclusion

The present experimental work and subsequent analysis demonstrate that a pure elongational flow is not guaranty in the strings of a beads-on-strings pattern formed during the breakup of free cylindrical-dilute-polymer-solution jets. One of the reason is that the successive regimes of small-scale dynamics exhibit short durations that sometimes are of the same order of magnitude as the characteristic time we want to measure or even less. Thus, the elongational flow has no time to properly settle and the corresponding elongational regime is unidentifiable. All this act as a brake upon the determination of dilute-polymer-solution relaxation time from the behavior of low-velocity cylindrical jets.

These results might explain some dependences between the relaxation time t_r and the injection conditions reported in the literature. Indeed, the regimes of the small-scale dynamics are recognized by their expected temporal variation. However, their small duration associated with small variations of the scale of interest might generate confusion between the tracked mathematical behaviors. In a previous work [11], we suggested a possible link between a bead coalescence mechanism along the jet and the dependence between t_r and the operating conditions. The simulation work due to Li and Fontelos [16] demonstrates that the coalescence mechanism doesn't modify the liquid strings' dynamics. Therefore, this mechanism is not responsible for the hypothetic presence of an EC regime. This, of course, doesn't exclude the fact that the absence of such a regime modifies the coalescence mechanism.

A confident measurement of the dilute-polymer-solution relaxation time from a jet experiment is possible. This is what this work demonstrates. It is not clear yet which association of diameter and velocity should be recommended to perform this measurement, but the experimental work presented here might define the bases of a protocol to perform it with no ambiguity. The two important aspects of this protocol are 1 – the use of free liquid jets (meaning that it can be applied on any ligamentary structures whatever their production process); 2 – the use of a multi-scale description tool that straight-forwardly applies in any conditions.

References

[1] Rodd, L.E., Scott, T.P., Cooper-White, J.J., & McKinley, G.H. *Applied Rheology* 15: 12-27 (2005)
[2] Campo-Deño, L., Clasen, C., *Journal of Non-Newtonian Fluid Mechanics* 165: 1688-1699 (2010)
[3] Oliviera, M.S.N., McKinley, G.H., *Physic of Fluids* 17: 071704 (2005)
[4] Schümmer, P., Tebel, K.H., *Journal of Rheology* 26: 77-78 (1982)
[5] Schümmer, P., Tebel, K.H., *Rheologica Acta* 21: 514-516 (1982)
[6] Schümmer, P., Tebel, K.H., *Journal of Non-Newtonian Fluid Mechanics* 12: 331-347 (1983)
[7] Bazilevsky, A.V., Entov, V.M., Rozhkov, A.N., Yarin, A.L., *Third European Rheology Conference and Golden Jubilee Meeting of the British Society of Rheology*, Springer, Dordrecht: 44-46 (1990)
[8] Keshavarz, B., Sharma, V., Houze, E.C., Koerner, M.R., Moore, J.R., Cotts, P.M., Threlfall Holmes, P., McKinley, G.H., *Journal of Non-Newtonian Fluid Mechanics* 222: 171-189 (2015)
[9] L. Rayleigh, *Proceedings of the London mathematical* 10: 4-13 (1879)
[10] Tirel, C., Renoult, M.C., Dumouchel, C., Lisiecki, D., Crumeyrolle, O., Mutabazi, I., *Journal of Non-Newtonian Fluid Mechanics* 245: 1-10 (2017)
[11] Tirel, C., Renoult, M.C., Dumouchel, C., Blaisot, J.B., *Ilass Europe 28th european conference on liquid atomization and spray systems*, Valencia (2017)
[12] Dumouchel, C., Aniszewski, W., Vu, T.T., Ménard, T., *International Journal of Multiphase Flow* 92: 181-192 (2017)
[13] Dumouchel, C., *ASME 2017 Fluids Engineering Division Summer Meeting*: FEDSM2017-69590 (2017)
[14] Evers, L.W., *SAE Technical Series* 940190 (1994)
[15] Stelter, M., Brenn, G., Yarin, A.L., Singh, R.P., Durst, F., *Journal of Rheology* 44: 595-616 (2000)
[16] Li, J., Fontelos, M.A., *Physics of Fluids* 15: 922-937 (2003)